PHYSICAL REVIEW B VOLUME 41, NUMBER 16 1 JUNE 1990

Influence of contact angle on quasistatic fluid invasion of porous media

Marek Cieplak* and Mark O. Robbins
Department of Physics and Astronomy, Johns Hopkins University, Baltimore, Maryland 21218

(Received 28 June 1989; revised manuscript received 27 December 1989)

We present results of detailed simulations of capillary displacement in model two-dimensional porous media as a function of the contact angle θ of the invading fluid. In the nonwetting limit ($\theta = 180°$), growth patterns are fractal as in the invasion percolation model. As θ decreases, cooperative smoothing mechanisms involving neighboring throats become important. The typical width of invading fingers appears to diverge at a critical angle θ_c, which depends on porosity. Above θ_c the invaded pattern remains fractal at large scales. Below θ_c the fluid floods the system uniformly. Probabilities of local interface instabilities are analyzed to elucidate these findings.

I. INTRODUCTION

Fluid invasion, displacement of one fluid by another in porous media, is important in a large number of industrial and natural processes.[1,2] Examples include displacement of oil by water in underground reservoirs, and spread of water or hazardous chemicals through soil or concrete. In recent years, fluid invasion has also proved a fertile field for fundamental studies of pattern formation in growth.[3-8] As the velocity, viscosity, and pore geometry are varied, the pattern formed by the invading fluid changes from compact to dendritic[3] or to a fractal characteristic of either percolation[4-6] or diffusion limited aggregation.[7,8] Changing the wetting properties of the fluids may change the structure from self-similar to self-affine.[9]

Lenormand and Bories[5] and Chandler *et al.*[6] have proposed a widely used model of fluid invasion known as the invasion percolation (IP) model. The model starts by separating the pore space into larger regions called "pores," and "throats" which connect them. The topology of this network can be described by a set of nodes corresponding to each pore, connected by bonds corresponding to each throat.

In the IP model, fluid invasion is mapped onto the problem of percolation[2,10] on the network of pores and throats. When the invading fluid is nonwetting (NW), the pressure P required to push an interface through a throat increases as the throat becomes *smaller*. When the invading fluid is wetting (W), the required P increases as the opening becomes *larger*. Since the largest openings are pores, they will be the hardest regions to pass in W invasion.

In either case, the number of pores or throats which the interface can pass through depends on P. One can think of passable pores or throats as occupied nodes or bonds on the corresponding network. The regions that could be invaded correspond to connected clusters on this network. Increasing P increases the number of occupied nodes or bonds. Conventional percolation theory[10] can be used to predict how the size of invadable regions increases with P, and to determine the critical value P_c where the fluid can invade from one side to the other of an infinite medium.

Several aspects differentiate the IP model from usual percolation. The first is that the invading fluid can only reach clusters connected to the region where it enters the medium. In contrast, in usual percolation one considers all clusters. A more important distinction arises when the displaced fluid is incompressible. Then any region surrounded by the invading fluid is trapped: There is no path for the displaced fluid to leave and the invading fluid cannot penetrate into the region no matter how high the pressure. Trapping depends on the history of growth and decreases the size of invaded clusters. Studies indicate that trapping is important in two-dimensional (2D) systems,[2] where it may change the fractal dimension of the invaded clusters.[11]

In usual percolation the approach to the percolation transition is universal. It depends only on the dimension, not on the network structure or whether one considers percolation of sites or bonds. Thus studies of the IP model have not included the detailed geometry of the porous media. Rather, random numbers were assigned to represent the pressures at which different bonds or throats on a lattice could be invaded. Both bond percolation, which corresponds most closely to NW invasion, and site percolation, which corresponds most closely to W invasion, gave fractal invasion patterns with pore scale structure.[11]

The basic symmetry between W and NW invasion predicted by the IP model is at odds with experimental evidence. Studies of flows in etched networks of tubes,[12] and in thin Hele-Shaw cells packed with glass beads,[13] show significant broadening of patterns as the invading fluid becomes more wetting. When viscous and boundary effects are negligible, NW invasion produces a fractal pattern with pore scale fingers. In contrast, invasion by a wetting fluid produces interfaces which are nearly flat.[14] Even at high velocities, viscous fingers in the W case remain much larger than the pore size.[13] There appears to be a strong smoothing force analogous to a surface tension at long length scales.[9] Similar behavior is observed in invasion of porous rocks.[15]

Lenormand and co-workers[4,12] provided the first microscopic explanation for the large difference between W and NW invasion of etched square networks. They showed that the relevant growth mechanisms were different in the NW and W limits. In particular, independent pistonlike motion of a single meniscus through a throat was found to dominate NW invasion. Mechanisms involving a confluence of two or three menisci at tube intersections (pores) dominated W invasion. The latter mechanisms cannot be described by a simple percolation picture. There is no well-defined pressure at which a given throat or pore can be invaded. The pressure depends on the configuration of the interface; that is, on the other invaded regions.

This experimental evidence led us[16] to construct a model of fluid invasion which explicitly included the microscopic geometry of the porous medium and the wetting properties of the invading fluid. The wetting properties determine the contact angle θ at which the fluid interface intersects the porous medium.[17] We choose to measure θ through the invading fluid so that $\theta = 180°$ and 0° correspond to NW and W invasion, respectively. The porous media was modeled by a 2D array of disks with random radii (see Sec. II A), and simulations were done in the quasistatic limit where capillary forces dominate viscous ones.

In the perfectly NW case, $\theta = 180°$, the interfaces produced were similar to the fractal patterns of the IP model. Each segment of the interface advanced almost independently, and the mean width of invading fingers, $\bar{w}$, was of order the pore size. As θ decreased, $\bar{w}$ diverged at a critical angle θ_c. The interface contained longer and longer flat segments. This smoothing was shown to result from the increasing importance of cooperative invasion of neighboring pores. Like the mechanisms observed by Lenormand *et al.*,[12] these cooperative mechanisms cannot be described by percolation models.

Above θ_c gradual increments in P could still yield stable percolating patterns at a critical pressure P_c. Below θ_c, cooperative invasion led to a qualitative change in the invasion process. Increasing P destabilized larger and larger connected segments of the interface. Above a critical P_c, the entire interface became unstable and the system was flooded in a compact pattern. We have shown that this growth is consistent with a critical depinning transition rather than a percolation transition.[9] Our findings can be summarized by the generic phase diagram[9] shown in Fig. 1. In the region labeled "static," there are many possible stable interfaces. In the region labeled "moving," no *infinite* interface is stable. (There may, of course, be small closed interfaces in locally unfavorable regions which would be stable.)

In this paper, we present results of comprehensive studies of the percolationlike invasion patterns obtained for $\theta > \theta_c$. (For clarity we will only use the term "percolation" to describe fractal growth characteristic of a percolation transition rather than simply to imply spanning of the system.) We start, in Sec. II, by describing the model porous systems used in our studies. These systems are all 2D arrays of solid disks with random radii. Section II also describes in detail how individual segments of the interface are calculated, how unstable segments are identified, and how they are advanced. In Sec. III we present our results. We first discuss percolation patterns obtained in the perfectly NW limit and show that they are indeed fractal. We then consider how the invaded pattern changes as θ decreases, and analyze the divergence of the finger width. These results are correlated with changes in the probabilities of microscopic instabilities in Sec. IV. We close in Sec. V by offering some concluding remarks.

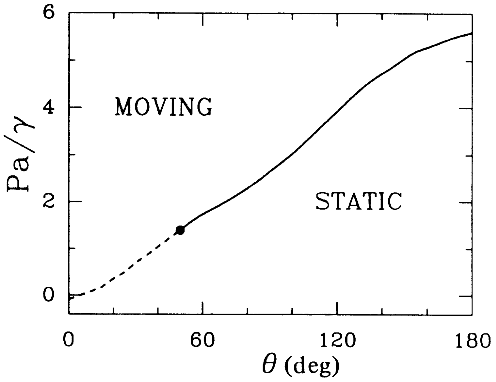

FIG. 1. The phase diagram for quasistatic invasion of system A (defined in Fig. 2) as a function of the dimensionless pressure aP/γ and θ. A solid line indicates the critical pressure for the percolation transition, and a dashed line the pressure of the depinning transition. Filled circles indicate the critical angle which separates the two types of critical behavior. The diagram is symmetric under the interchange $P \rightarrow -P$ and $\theta \rightarrow (180° - \theta)$ which corresponds to redefining the direction of motion. Similar phase diagrams are found for the other systems illustrated in Fig. 2.

II. MODEL

A. Porous media

To model the nearly 2D flow observed in Ref. 13, we use a 2D array of disks with random radii. This should be similar to a cross section through a random bead pack, and allows for a full solution for the interface shape. In 2D, the interface consists of circular arcs connecting disks. In 3D, interfaces are complex curved surfaces, which are not amenable to an exact analysis.

Despite its simplicity, this model has several advantages over tube network models. There is no artificial division of the pore space into throats and pores. The orientation of solid walls varies continuously, rather than discontinuously at the juncture between tubes. Such discontinuities can artificially decouple neighboring throats.

For simplicity we place the disks on a triangular or square lattice with lattice constant a. There are L atoms per row and L rows on the lattice with L between 300 and 1300. Thus the overall dimensions are La by La for square lattices and La by $La\sqrt{3}/2$ for triangular lattices. Figure 2 shows fragments of four distinct $L = 300$ systems which were studied. Radii were uniformly distributed within the intervals indicated in the figure and in Table I.

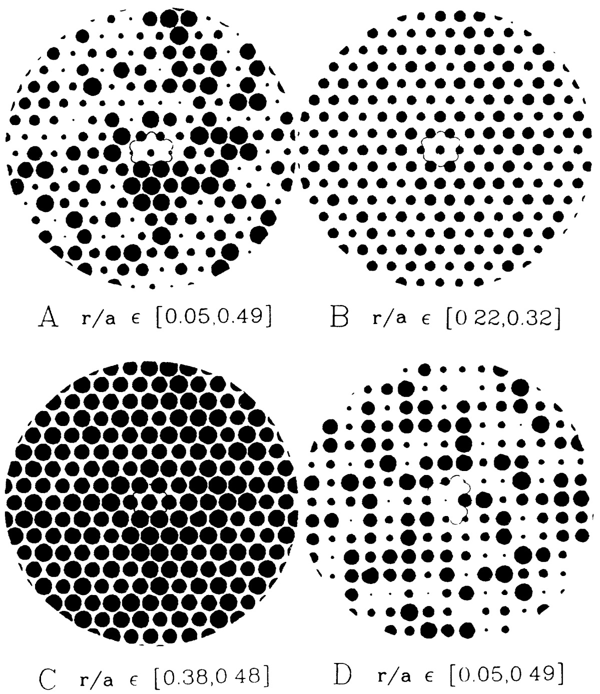
A r/a ∈ [0.05,0.49] B r/a ∈ [0.22,0.32]

C r/a ∈ [0.38,0.48] D r/a ∈ [0.05,0.49]

FIG. 2. Small sections from the 2D porous media used in our simulations. Disks are on a triangular lattice in systems A, B, and C, and on a square lattice in D. The lattice spacing is a. Radii r are randomly distributed within an interval. In samples A and D the interval is large, $r/a \in [0.05,0.49]$. For B, the mean radius is the same but the range is small, $r/a \in [0.22,0.32]$. For C, disks with the mean radius nearly touch, $r/a \in [0.38,0.48]$. Small initial interfaces are shown in the center of each sample.

All of the invasion patterns shown in this paper were obtained for system A which is the most disordered. The porosity Φ, defined as the fraction of area not covered by disks, is 0.67 in this system. The average radius of disks in system B is the same, but the dispersion is reduced. This makes the porous network much less random and more spacious: $\Phi = 0.73$. System C has the same dispersion as B, but a larger mean radius. This decreases the throat sizes and gives the lowest porosity, $\Phi = 0.32$. System D has radii in the same range as in system A, but the disks are placed on a square lattice. Here, $\Phi = 0.71$, which is roughly halfway between the values for A and B.

The network describing the pore space is the dual lattice of the lattice of disk centers. In the triangular systems, the triangular pores between disks lie on the vertices of a honeycomb lattice. The throats between disks connect nearest-neighbor vertices. For system D, the pores and throats form a square lattice with nearest-neighbor bonds. In analyzing the width and area of invaded regions we consider only the number of pores invaded. This corresponds to counting the number of sites on the dual lattice which are covered by the invading fluid.

TABLE I. Parameters of systems studied. Quoted values of θ_c and ν are those used in Fig. 13. Uncertainties in these values are discussed in the text.

System	Range of radii	Porosity	θ_c	ν
Triangular A	$[0.05,0.49]a$	0.67	49°	2.1
Triangular B	$[0.22,0.32]a$	0.73	69.715°	1.8
Triangular C	$[0.38,0.48]a$	0.32	20.5°	2.1
Square D	$[0.05,0.49]a$	0.71	59°	2.1

We have also studied systems in which the disk centers were randomly shifted from lattice sites. This decreases the influence of the symmetry of the lattice, but increasing the variation in radius has a similar effect. The variations with θ exhibited the same trends as the systems described below.

Several generalizations of the model can easily be made. We have not considered the case where disks overlap. Allowing this may help to simulate the effects of grain consolidation[18] which occurs in sintered bead packs or sandstones. Real porous media often contain many minerals with different wetting properties. One can model this by assigning disks different contact angles. Such generalizations will be considered in future work.

B. Fluid interface geometry

The interface consists of a sequence of arcs between pairs of disks. Stable interfaces at a fixed pressure drop P consist of arcs with radius γ/P, where γ is the coefficient of surface tension between fluids. Each arc must also intersect both disks at the proper contact angle θ.

Figure 3 shows examples of stable arcs for several contact angles. Dashed lines indicate the arc at the highest pressure $P_{\max}$ where a stable interface exists. At higher pressures, the interface is too curved to intersect both disks at the proper θ. Solid lines show arcs for $P = P_{\max}/2$ and $P_{\max}/4$ at each θ.

Note that for NW invasion, $\theta = 180°$, all arcs are hidden within the throat between the two disks. In contrast, arcs for W invasion, $\theta = 0°$, spread around the disks. These arcs are more likely to intersect neighboring arcs

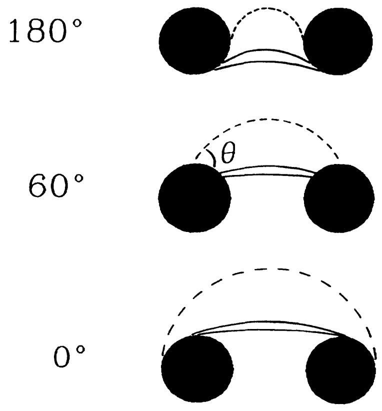

FIG. 3. Interfacial arcs between two identical disks of radius $0.25a$ for the indicated contact angles θ. The last stable arc at $P_{\max}$ is marked by a dashed line. Solid lines correspond to arcs for $P_{\max}/2$ and $P_{\max}/4$. $P_{\max}$ decreases from $4\gamma/a$ at $\theta = 180°$ to $4\gamma/3a$ at $\theta = 0°$.

and become unstable. This is the origin of the cooperative smoothing mechanism mentioned in the Introduction.

Consider two disks whose centers are, in general, a distance d apart. The geometry and notation used is shown in Fig. 4. Let the left- and right-hand side disks have radii r_1 and r_2, respectively. The contact angles may also differ, and we denote them by θ_1 and θ_2. The arc of radius r_p between disks is characterized by its center (x_c, y_c) on the x-y plane, and by the points at which it contacts the disks. These points are specified by angles ϕ_1 and ϕ_2 measured clockwise from the axis joining the disk centers.

Let β denote the angle between the two contact points as seen from the arc center, and b the difference in their y (vertical) coordinates. It is straightforward to show that

$$\phi_2=\phi_1-\theta_1-\theta_2+\beta+2\pi \ , \tag{1}$$

$$b=r_1\sin\phi_1-r_2\sin\phi_2 \ , \tag{2}$$

$$b=[d-r_1\cos\phi_1-r_2\cos(\pi-\phi_2)]\tan\mu \ , \tag{3}$$

$$b=2r_p\sin\mu\,\sin(\beta/2) \ , \tag{4}$$

with

$$\mu=\theta_1-\phi_1-\pi/2-\beta/2 \ . \tag{5}$$

Equations (2)–(4) allow us to solve for β and ϕ_1. Simplifying to the case $\theta_1=\theta_2=\theta$, we find

$$d(1-\rho^2\cos^2\eta)^{1/2}+2r_p\sin\beta/2=(r_1+r_2)\sin\eta \ , \tag{6}$$

$$\cos(\phi_1+\eta)=\rho\cos\eta \ , \tag{7}$$

where $\eta=\beta/2-\theta$ and $\rho=(r_1-r_2)/d$. Equation (6) can be reduced to a biquadratic equation which facilitates the calculation of η and hence β. Once ϕ_1 is obtained, from Eq. (7), the coordinate ϕ_2 of the other contact point is readily obtained from Eq. (1). The center (x_c, y_c) can also be readily calculated given the coordinates of bead centers.

For $P > P_{\max}$ there is no solution to the above equations, and no stable arc between beads. This segment of the interface is temporarily represented by the arc calculated for $P_{\max}$. Values of ϕ_1, ϕ_2, x_c, and y_c are used to check for other instabilities of the interface as described in the next subsection.

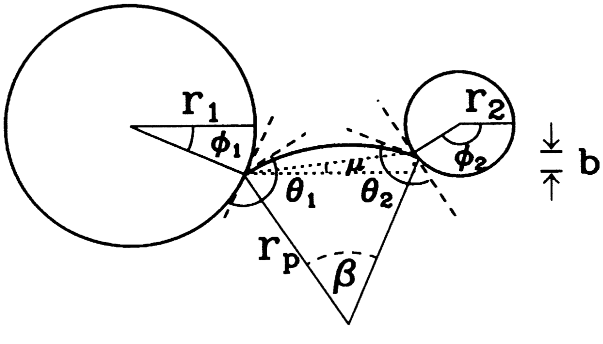

FIG. 4. Geometry used to calculate interfacial arcs. The distance between the centers of two disks is d.

C. Instabilities and growth mechanisms

The growth algorithm used is the same as in Ref. 16. Consider an initial interface which is stable at an applied P. Increasing P above a threshold value will cause a section of the interface to become unstable and initiate flow. In principle flow should be simulated by solving for the viscous pressure drop in the medium, and integrating the velocity for each section of the interface. However, in the quasistatic limit and at constant P, the interface moves rapidly between nearly stable configurations of the interface. One may model the dynamics as a stepwise process where each unstable section of the interface moves to the next stable or nearly stable configuration in turn. Growth continues until a stable interface is found, or the system is flooded.

Detailed examination of microscopic configurations of the interface reveals three basic types of instability (Fig. 5):[16]

(1) "burst"—there is no stable arc connecting two disks ($P > P_{\max}$);

(2) "touch"—the arc connecting two disks intersects another disk at the wrong θ, or extends beyond a disk which has not yet been on the interface;

(3) "overlap"—two neighboring arcs on the interface intersect.

Burst instabilities are eliminated by moving the interface forward to connect to the nearest disk as shown in Fig. 5(a). This disk is selected so that its center is closest to the center of the arc evaluated for $P=P_{\max}$, and lies in the angle subtended by this arc (Fig. 4). Two new arcs are created between the new disk and each of the original disks.

When the initial disks are nearest neighbors on the

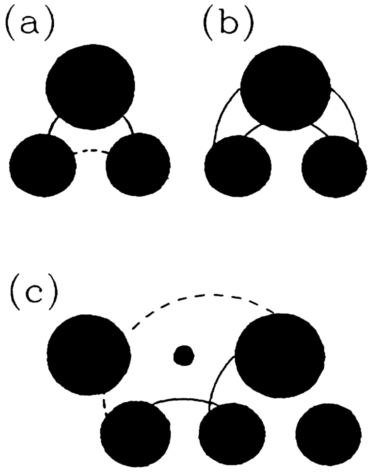

FIG. 5. Local mechanisms of growth. In each case the lower arc or arcs are unstable and growth is upwards. Dashed lines indicate arcs which would burst and thus are drawn at $P=P_{\max}$. Panel (a) illustrates burst of an unstable arc to connect to the disk in front of it. Panel (b) shows an arc which touches the upper bead, and the two new arcs created. Panel (c) shows two overlapping arcs being replaced by one arc connecting two extremal disks. The new arc is unstable against touches and burst.

square lattice, the above prescription is ambiguous. There are two equidistant neighbors which form the other corners of the square whose base is formed by the initial disks. For the relevant range of θ, we found that bursting to either corner always produced an unstable arc across the diagonal. This in turn led to filling of the entire square. We thus simplified the procedure by replacing the initial arc by three arcs surrounding the square in one step.

Touches are a local mechanism which are very similar to bursts. Unlike bursts, however, occurrence of touches depends on the size of the forward disk and thus on the *direction* of flow. Touches are eliminated by replacing the initial arc with two arcs connecting the initial disks to the touched disk [Fig. 5(b)]. To identify touches we check disks within the angle subtended by the initial arc. If the sum of the arc and disk radii is larger than the distance between arc and disk centers, the disk is "touched." If several disks satisfy this condition, the one closest to the arc center is chosen.

The removal of overlaps proceeds as shown in Fig. 5(c): The disk which is common to the intersecting arcs is removed from the interface. Two distinct types of overlap can occur. Figure 5(c) shows two arcs which overlap on a disk—the points where the arcs hit the disk have moved past each other. Arcs may also intersect in the pore space. The former case is most likely for W invasion where the arcs extend around the disks. The latter only occurs in NW invasion where the interfaces are more curved (higher P) and avoid contact with the disks. Overlap on disks plays the crucial role in changing the growth pattern as θ decreases. Overlap in the pore space has less effect, but is included for completeness.

Both types of overlap depend strongly on the interfacial angle α between the axes connecting successive pairs of disks along the interface. We measure this angle through the displaced fluid, so that in Fig. 5(c) $\alpha=120°$. It is evident from the figure that if α were decreased, the arcs would overlap more, while if α were sufficiently increased, overlap would cease. On the hexagonal lattice $\alpha=n\times 60°$ if both arcs connect nearest neighbors. Arcs between more distance disks give rise to other values of α, but are generally less important except at very small θ.

Testing for overlap on disks is done in the following manner. Suppose the arc between disks $(m-1)$ and m contacts disk m at ϕ_2, and the arc between m and $(m+1)$ contacts disk m at ϕ_1 $(0<\phi_i<2\pi)$. These angles are calculated relative to the axes connecting the respective pairs of disks. Since these axes differ by an angle α, the arcs overlap on disk m if $\phi_2-\phi_1<\alpha-\pi$.

Overlap in the pore space only occurred for $\alpha\leq 90°$. One condition for this type of overlap is that the distance between the centers of successive arcs is less than the sum of their radii. The second is that the angles subtended by the arcs overlap. This was always true for $\alpha\leq 90°$. Thus only the first condition needed to be checked.

D. Growth algorithm

The interface was specified by the sequence of disks connected by consecutive arcs. Growth was initiated from a ring around a disk near the center of the porous media. This avoided effects due to container walls, which possess their own wetting characteristics. It also simplified analysis of the fractal dimension of invaded patterns.

The interface was initially stable at some applied P. P was then increased by a small step, and all resulting instabilities on the interface were identified. Stability against bursts and touches does not depend on the configuration of other arcs. If these local instabilities were detected, we set a flag determining the new disk to which the interface would connect. We also tested for overlaps and set a similar flag. Since overlaps depend on neighboring arcs, the angles ϕ_i were stored.

We then proceeded to remove instabilities through the local changes described in the preceding subsection. Starting from some point on the interface, instabilities were removed sequentially around the interface. Each time a new arc was created, it was tested for stability. Any new instabilities were not removed until the remainder of the interface was traversed, and preexisting instabilities were removed. This process continued until all arcs on the interface were stable.

In some cases a given arc had several types of instability. For example, in Fig. 5(c) the final arc would burst, and it also touches the two disks on the upper left. Touches imply that the calculated arc has advanced too far. In Fig. 5(c), the arc must pass through two disks before reaching the configuration shown. Thus the invading fluid would touch the nearest disk before reaching the bursting configuration. For this reason touches must be eliminated first. Overlaps also imply that the arcs have moved too far forward. They were eliminated before bursts, but after touches. Examination of many possible interface growths showed that this hierarchy always led to physically reasonable growth kinetics.

Advancing an unstable arc may cause it to intersect a nonadjacent arc. This forms a closed loop around the invaded fluid. As in the IP model,[5,6,11] we assume that the fluid trapped in such loops is incompressible. Then no further growth can occur and the loop is removed from the interface. Growth is also stopped when the interface reaches the boundary of the system.

When a stable interface was obtained, the pressure was again incremented, until the invading fluid spanned the system. Small increments in P were used to simulate quasistatic motion. The sequence of P's did not change the main characteristics of the invaded pattern, but did change the fraction of trapped fluid slightly.

The pressure required to span the system depended on the central starting ring, as expected from a percolation model. If one starts in an unfavorable region, large pressures are needed to overcome the local barriers. Once these are overcome, P is sufficiently high that the fluid can invade almost all throats. In percolation models, one must start on the infinite percolation cluster to span the system at the lowest possible P. We thus varied the location of the central starting ring until the system was spanned at the lowest P.

For large θ one may start from rings of unit radius, as shown in Fig. 2. In the vicinity of θ_c, starting rings of radius $\geq 10a$ were needed to produce stable percolating interfaces. Otherwise the pressure to initiate flow exceeded the percolation pressure P_c. As shown below, invasion is correlated over an increasing length scale as $\theta \rightarrow \theta_c$. The starting ring must be larger than this characteristic scale to allow correlations in the initial stages of growth. If it is not, the pressure required to initiate growth is greater than P_c. This dependence on the size of the starting ring is related to the effective surface tension observed below θ_c in recent work.[9] As discussed in Sec. III C, using a finite starting ring always increases the pressure needed to span the system when $\theta < \theta_c$.

This growth algorithm differs in several ways from the IP model.[4–6] The microscopic configuration of the interface is not calculated in IP. Instead each throat is assigned a critical pressure where the arc becomes unstable, which is independent of the configuration of the interface and the direction of invasion. In general, this model can only describe bursts. Touches depend on flow direction, and overlap is a cooperative mechanism which depends on both flow direction and the configuration of adjacent arcs. As shown below, this cooperative character leads to large changes in the growth morphology.

Another difference is that in the IP model growth occurs at the least stable throat at each step, while we advance all instabilities together. Both algorithms are relevant to experiments. The IP algorithm corresponds to growth at constant infinitesimal flow, while our algorithm corresponds to growth at constant P. The IP algorithm has the important advantage of automatically seeking out the infinite percolating cluster and P_c. If one starts at an unfavorable site, the pressure will automatically rise to overcome local obstacles. When the fluid reaches the infinite percolating cluster, the pressure will decrease to reflect the lower barriers. In our algorithm, we must search for appropriate starting sites as described above. However, the computational effort to determine whether there is an instability or not is substantially less than that to determine at what P each possible instability will occur. We compare the types of patterns produced by these two algorithms in the NW limit below.

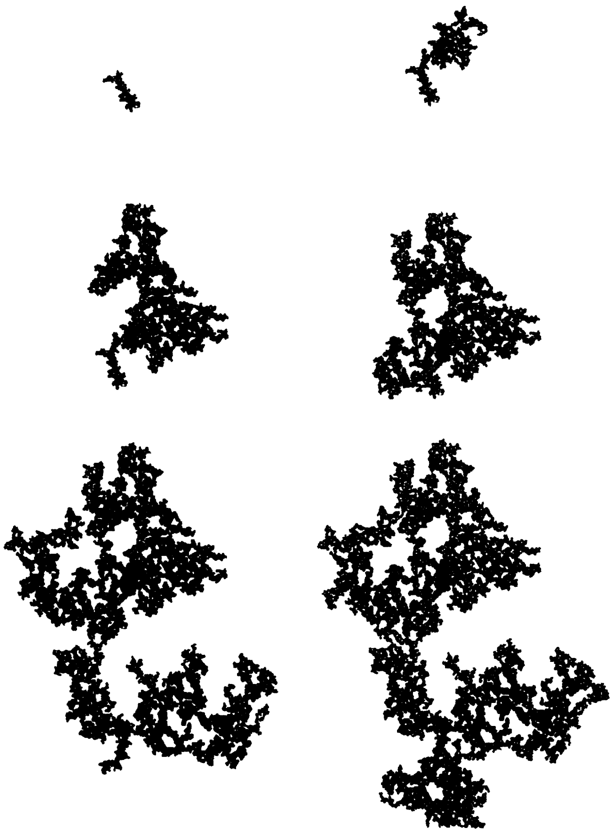

FIG. 6. Stages of growth in an $L = 300$ sample of system A at $\theta = 179°$, where $P_c = 5.585\gamma/a$. The deviation from criticality, $(P_c - P)/P_c$, for clusters of increasing size was equal to 0.194, 0.069, 0.047, 0.033, 0.026, and 0.022, respectively.

III. RESULTS

For a uniform system (equal radii) our algorithm always yields a regular faceted pattern with the lattice symmetry, which is in agreement with experiment.[3] The pattern formed in disordered systems depends strongly on the contact angle, as described below.

A. Nonwetting invasion

In the NW limit, growth is well described as percolation. Figure 6 shows several stages in the growth of the final percolating cluster shown in Fig. 7. As with the following patterns, system A is shown, but results for other systems are similar. The value $\theta = 179°$ rather than 180° was used to represent NW invasion for numerical reasons.

For system A, the critical pressure $P_c = 5.585\gamma/a$. The largest cluster shown in Fig. 6 was obtained at $P = 5.46\gamma/a$. Each increment in P was small enough that only a few arcs on the interface became unstable. The pressure increments decreased as $P \rightarrow P_c$, but the resulting invaded regions are noticeably larger. As discussed in Ref. 9, the area invaded when a single arc becomes unstable diverges as $P \rightarrow P_c$. The exponent can be

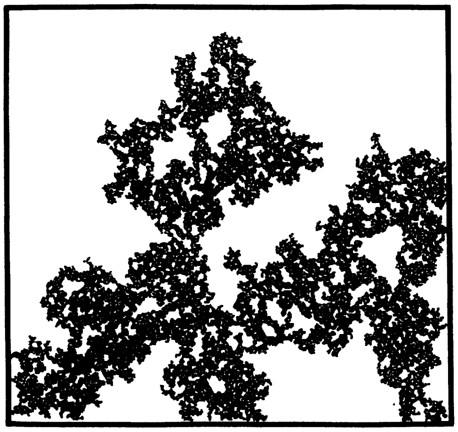

FIG. 7. The percolating cluster obtained as the final stage of growth in the sample of Fig. 6.

related to percolation theory.

In this NW limit, growth occurs almost exclusively by bursts. At a given P, the interface can only move through throats whose width is greater than $2\gamma/P$. As noted above, the network of throats forms a honeycomb lattice. On this lattice, bond percolation occurs when 65% of the bonds are present,[10] *if the presence of neighboring bonds is uncorrelated.* We find that the fraction of throats which can be invaded at P_c is 0.71 ± 0.01 for systems A, B, and C. We attribute the small discrepancy to correlations between throats: The size of one disk affects the six surrounding throats. The effect of correlations is stronger for the square lattice. We find that 60% of throats can be invaded at P_c, whereas the bond percolation probability is 0.5.

As a further illustration that bursts control NW invasion, media with radii in the ranges for systems B and C were obtained by rescaling the radii of each disk in the medium shown in Figs. 6 and 7. This maintains the hierarchy of relative throat sizes which control bursts, but would affect the other instabilities. The percolating patterns in these media at $\theta=179°$ are identical to the one presented in Fig. 7. The only change is in the value of P_c. For the highly porous system B, $P_c=4.604\gamma/a$, and for the denser system C, $P_c=17.47\gamma/a$.

In a percolation picture, the invaded pattern in Fig. 7 represents the percolating cluster of connected bonds. Some of the bonds are missing because trapping stops growth into surrounded regions. However, this only affects the inner regions, not the outside interface of the cluster. Growth starting from any site on the cluster should reproduce it, except for changes in the trapped regions near the initial site. We find that the pattern shown in Fig. 7 is indeed nearly reproduced for any starting ring on the invaded area. At $P=P_c$, the only differences are in the trapped regions near the starting ring. Growth from any ring which is not on the invaded area will not overlap this area until P exceeds P_c. Such starting rings are on finite clusters in the percolation picture. Starting from such locally unfavorable regions may increase the P needed to span the system by as much as a factor of 2.

The most convincing evidence that the invaded patterns in the NW limit represent percolation comes from analyzing their large-scale fractal structure. This fractal character is evident in Fig. 8, which shows the pattern invaded using our algorithm in a system with $L=1000$. Figure 9 shows the invaded pattern in the same medium using an algorithm more like IP where the most unstable arc (widest throat) was advanced at each step. The algorithm differed from IP in two ways. First, as noted above, the widths of neighboring throats are correlated because they depend on the same disk radius. More importantly, in IP simulations growth stopped as soon as the pattern spanned the system. We continued growth until all throats which were more unstable than the critical percolating throat width had been invaded. Thus the *external* interface is identical to the one shown in Fig. 8. However, since the IP-like algorithm allows some regions of the interface to get far ahead of others, more fluid is trapped.

The fractal dimensionality d_f of invaded patterns was determined in three ways. First, we found the invaded area inside circles of increasing radius r about the center of mass. Each pore is associated with a site of the dual honeycomb lattice. The area was found by counting the number of sites on this lattice which corresponded to invaded pores. Trapped regions were excluded, and results were averaged over four different $L=1000$ patterns. The number of invaded pores $M(r)$ is plotted on a logarithmic scale in Fig. 10. Over a little less than a decade in r, the data for both growth algorithms lie on straight lines whose slope $d_f=1.89\pm0.02$. This is consistent with the value[10] for normal percolation $d_f=91/48\simeq1.896$. Lines with the latter slope are plotted in the figure. The cutoff in $M(r)$ at large scales is a result of finite system size. Deviations at small scales are related to the finite finger width described below. There is also less self-averaging at small scales.

We also calculated the length of the total interface (internal and external) as a function of the length of the measuring "yardstick." The scaling with yardstick

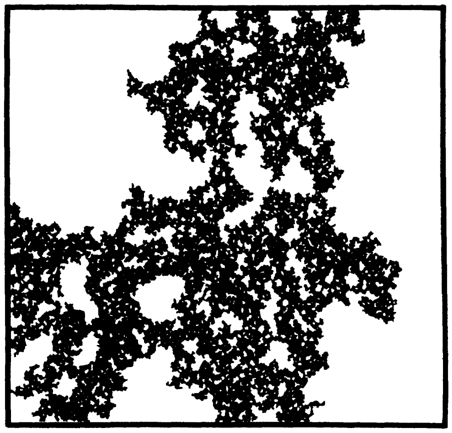

FIG. 8. The percolating cluster in an $L=1000$ sample of system A for $\theta=179°$. The central 300×300 array of disks had the same set of radii as in Fig. 6.

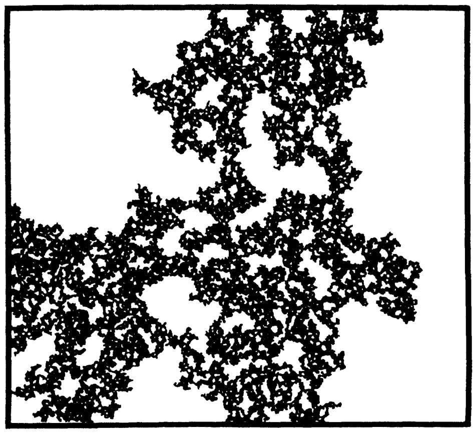

FIG. 9. The percolating cluster at $\theta=179°$ for the sample of Fig. 8, but grown with an invasion percolationlike algorithm.

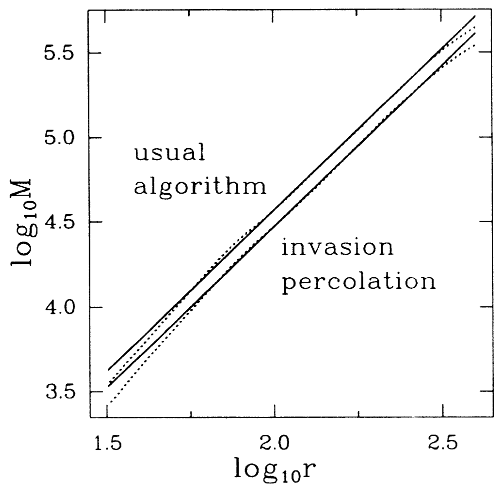

FIG. 10. The scaling of "mass" vs radius for $L = 1000$ samples of system A. The upper dotted line shows results averaged over four samples grown with our usual growth algorithm. The lower dotted line shows results averaged over three samples grown with the invasion percolationlike algorithm. The solid lines are fits with slope 1.896, which is the value of d_f for normal percolation.

length gives the caliper dimension of the interface[2] which equals d_f for self-similar fractals. Our results for both growth algorithms, $d_f = 1.89 \pm 0.04$, were consistent with the value of d_f obtained from $M(r)$.

Finally, we evaluated the box dimension of the clusters.[2,19] This was smaller, $d_f = 1.84 \pm 0.03$, than the other values. However, analysis of normal percolation clusters on comparable size square lattices also gave smaller values $d_f = 1.86 \pm 0.03$, and previous work indicates that this measure is often too small.[19]

Thus all our results for d_f are consistent with the fractal dimension of normal percolation. While one might expect d_f to be universal, Wilkinson and Willemsen[11] found different values for IP clusters in 2D: $d_f = 1.82$ for honeycomb and square lattices, and 1.88 for triangular lattices. Our data are clearly inconsistent with the value 1.82, and consistent with the value for normal percolation. Since both of our growth algorithms gave the same d_f, the discrepancy does not result from the order in which instabilities are advanced. However, it may be that continuing growth after the pattern first hits the boundary increases d_f. Also, the IP simulations were actually done for random site probabilities rather than random bonds, and this may affect d_f if it is nonuniversal in 2D. A final possibility is that d_f is universal, but previous IP simulations were influenced by finite-size effects.

The conclusion of our studies of NW invasion is that they are well described by percolation ideas. The issue of possible variations in d_f remains open, but secondary.

B. Divergence of finger width as θ decreases to θ_c

We now consider how the invasion patterns evolve as θ decreases—the invading fluid becomes more wetting. For type-A samples, the pattern remains almost identical as θ changes from 179° down to 110°. Noticeable changes begin in the vicinity of 90°, and soon all similarities to the NW pattern are lost. Figure 11 shows $L = 300$ patterns obtained for $\theta = 70°$, 60°, and 58°. To isolate the effects of changes in growth mechanism, all figures are for the same set of disk radii as were used in Figs. 6 and 7. Note that the size of contiguous invaded regions, or fingers, becomes broader as θ decreases. The percolating pressures show a systematic decrease (e.g., $P_c = 1.677\gamma/a$ for $\theta = 58°$). Furthermore, the patterns generated turn out to be increasingly dependent on the position of the starting ring as well as on the history of applied pressures. It is no longer true that starting from different rings within an invaded pattern will reproduce the same pattern.

These observations provide evidence of marked

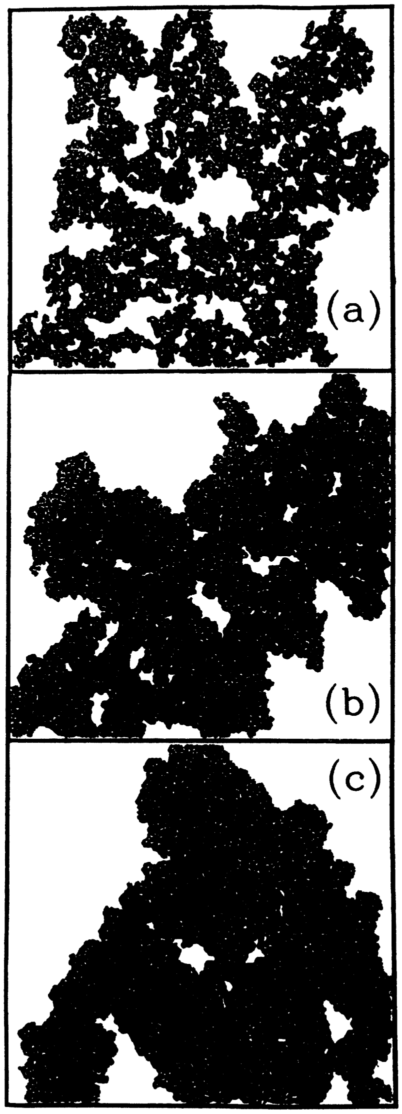

FIG. 11. Invasion patterns in the sample of Figs. 6 and 7 at (a) $\theta = 70°$, (b) $\theta = 60°$, and (c) $\theta = 58°$. The corresponding values of P_c are 1.995, 1.736, and $1.677\gamma/a$. The average finger widths $\bar{w}$ are 9.9, 31.9, and $53.7a$, respectively.

changes in the growth process, but are qualitative. Statistical measures of the growth are needed, which are independent of the particular realization of the porous media, the history of pressures, and the starting site. Several such measures can be derived from the distribution $D(w)$ of finger widths w.

To measure w, we make parallel slices through each pattern. The slices are along lines of nearest-neighbor disks, and the set of all slices covers the whole area of the system. These slices are broken up into segments which lie entirely within the invaded region. The width w of each segment is found by counting the number of adjacent invaded pores [which lie on the sites of the dual lattice (Sec. II A)], and multiplying by the pore spacing. For triangular lattices the pore spacing is $a/2$ and for square lattices it is a.

We found that the distribution $D(w)$ was generally well described by an exponential. At some values of θ there were deviations at small w, but the large w tail always had an exponential form. The mean value $\bar{w}$ at P_c gave the most reproducible measure of the width, and is plotted in Fig. 12. In general, fluctuations with the distribution of radii, choice of starting ring, sequence of pressures, and stage of growth (P) were of order 5%. Other measures of the width are discussed below.

For all systems studied, $\bar{w}$ increased markedly as θ decreased. For example, the finger width of the pattern shown in Fig. 11(c) is about 12 times larger than in the NW pattern of Fig. 7. The value of $\bar{w}$ appears to diverge at a critical angle θ_c. Dotted lines in Fig. 12 are guides to the eye which indicate the power-law divergence:[19]

$$\bar{w}(\theta) \propto (\theta-\theta_c)^{-\nu}, \tag{8}$$

with θ_c and ν equal to the values shown in Table I.[20]

Precise determination of θ_c and ν is difficult because both are unknown, and memory and computational time limited us to cases with $\bar{w} < 150$. While this allowed us to observe a decade and a half increase in $\bar{w}$, $\tau \equiv (\theta-\theta_c)/\theta_c$ changed by less than a decade. Even if θ_c were known exactly, we estimate that corrections to the leading order divergence could cause errors of order ± 0.2 in fits to ν. When θ_c is unknown, uncertainties are much larger.

In two systems we were able to place limits on θ_c that decreased our uncertainties in ν. In system A, we saw a clear depinning transition (see Sec. III C) at 45°, and percolation with $\bar{w}=144a$ at 54°. Extrapolating from both sides indicated $48° < \theta_c < 51°$. For this range of θ_c, best fits for ν were between 1.6 and 2.5. Figure 13 shows the best fit to the largest range of data points which gave $\theta_c = 49°$ and $\nu = 2.1$.

In system B we were able to find an exact lower bound, $\theta_c \geq 69.715°$, by examining the variation of the probabilities of different types of instabilities with P and θ. This will be explained in more detail in Sec. IV. Here we just mention that below 69.715° there is a range of P where no new instabilities occur, and that P_c lies in this gap. No gap occurs in other systems, so that similar bounds could not be found. If θ_c is equal to the lower bound, system B may be in a different universality class.

An upper bound for θ_c comes from the last data point in Fig. 12: $\theta_c < 72°$. We were unable to determine from our data whether θ is equal to the exact lower bound or a fraction of a degree larger. For $\theta_c = 69.715°$ the best fit to Eq. (8) gives $\nu = 1.8$. The data are reasonably fit for θ_c up to 70.5, where we find $\nu = 1.4$. As above, we estimate that corrections to the leading divergence might cause additional errors of order 0.2 in our determination of ν.

In Fig. 13 we show fits to Eq. (8) with $\nu = 2.1$ for systems A, C, and D, and $\nu = 1.8$ for system B. The corresponding θ_c's are listed in Table I. Given the uncertainties described above, all of our data could be fit with a universal exponent between about 1.7 and 2.2. We have

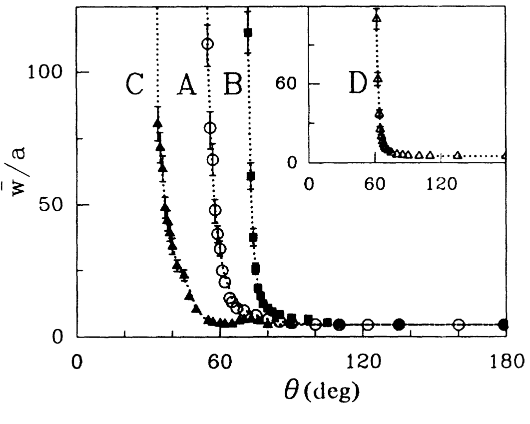

FIG. 12. Divergence of the finger width $\bar{w}$ as θ decreases for the four systems illustrated in Fig. 2. Error bars are indicated, and the dotted lines are guides to the eye indicating the power-law divergence. The value of θ_c appears to decrease monotonically with porosity. The data points corresponding to system D would be roughly halfway between those corresponding to A and B.

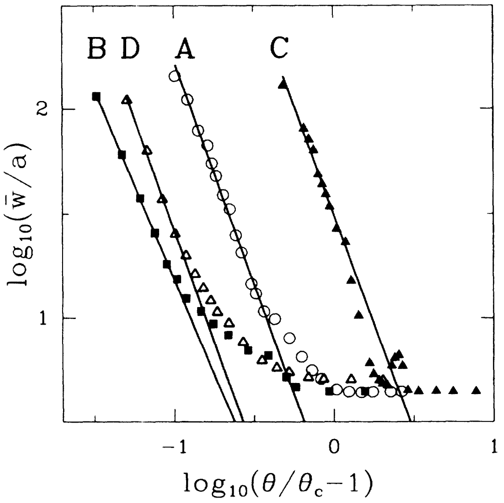

FIG. 13. Log-log plots of the data in Fig. 12. The straight lines have slopes 2.1 for systems A, C, and D, and 1.8 for system B.

chosen to use a different exponent for system B because of the difference in growth mechanisms. We hope to study simplified lattice models which include cooperative mechanisms. This would allow a more precise determination of ν, and a test of universality.

One may ask whether $\bar{w}$ is the only characteristic length in the invaded patterns. In order to answer this question we have studied other measures. The simplest of these is the dispersion, $\sigma_w \equiv [\langle (w-\bar{w})^2 \rangle]^{1/2}$, of the finger width distribution. For a perfect exponential distribution σ_w should equal $\bar{w}$. Another measure $\bar{\bar{w}}$, was defined as the decay length describing the exponential tail of $D(w)$. Still another scale may be defined by treating all trapped regions whose perimeter contains less than n disks as filled, and recalculating widths. This corresponds to using a less precise tool to study the structure. Average widths calculated in this manner are denoted by $\bar{w}_n$.

The above measures all involve cross sections of the pattern and are sensitive to the size and number of trapped regions. An independent measure can be obtained by studying correlations in the surface normal $\hat{n}$ of the external interface. For each arc, $\hat{n}$ is defined as the direction normal to a line between the centers of the connected disks. We define $S(l)$ as the average of the dot product between surface normals of all points on the interface which are separated by Cartesian distance l. This correlation function decays exponentially:

$$S(l) \sim \exp(-2l/\tilde{w}) \ . \tag{9}$$

The parameter $\tilde{w}$ characterizes length scales over which the interface turns over, and thus is also a measure of the finger width. [Note that S decays over a length of order the *radius* of curvature while $\bar{w}$ represents a characteristic *diameter*, hence the factor of 2 in Eq. (9).]

Figure 14 shows σ_w, $\bar{\bar{w}}$, $\tilde{w}$, and w_3 plotted versus $\bar{w}$ on a log-log scale. It is clear that all these lengths scale with $\bar{w}$ as $\theta \rightarrow \theta_c$. Similar results are found for $\bar{w}_n$ with $n > 3$. Thus a single length scale characterizes the diverging finger width in these simulations. Note however, that very close to θ_c we see some indication that $\bar{w}$ may saturate due to a fixed low density of trapped regions which occur during growth. We hope to explore this with larger simulations.

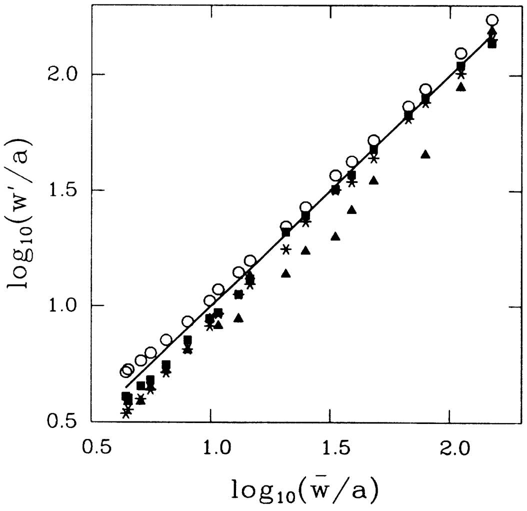

FIG. 14. Other measures of the finger width. Here, w' stands generically for the following: σ_w is the dispersion (squares), $\bar{\bar{w}}$ is the length characterizing the exponential tail of $D(w)$ (stars), $\bar{w}_3$ is the mean width when three-disk traps are considered invaded (circles), and $\tilde{w}$ is the length characterizing surface normal correlations (triangles).

In the NW limit, we found fractal structure characteristic of percolation at scales larger than $\bar{w}$ (Sec. III A). The patterns and growth mechanisms are almost unchanged in all systems as θ decreases from 179° to around 110°. At smaller θ, it is difficult to determine whether the large-scale structure remains percolationlike. Quantitative studies would require increasing system size with $\bar{w}$, which is beyond our current computer power. However, Fig. 15 provides an indication that the large-scale structure remains similar. Invaded patterns for the indicated values of θ have been scaled so that $\bar{w}/L$ is the same in each panel. The value of $\bar{w}$ varies by a factor of 8, but the qualitative structure of the patterns remains unchanged. Except for the spurious variation in the intensities of the black invaded regions, it is difficult to tell which picture is at which scale.

These results suggest that although the lower length scale cutoff in fractal scaling, $\bar{w}$, diverges as $\theta \rightarrow \theta_c$, the large-scale structure remains that of a fractal percolation pattern. While we have not ruled out a change in fractal dimension with θ, results on other systems suggest that this is unlikely for $\theta > \theta_c$. At θ_c, the fractal region is pushed out to infinity, and new large-scale structure can occur below θ_c. We now briefly describe the behavior below θ_c.

C. Invasion for $\theta < \theta_c$

Fluid invasion for $\theta < \theta_c$ is described in detail in Ref. 9. Here we merely summarize the results to elucidate the nature of the transition at θ_c. Suppose we start from an infinite stable interface at some P and θ, and increment P until a single arc on the interface becomes unstable. A segment of the interface around this unstable arc will advance as the interface moves to a new stable configuration. We define a correlation length ξ as the average Cartesian distance between the end points of the segments which advance. Above θ_c, ξ is nearly independent of P and provides yet another measure of the average finger width. Below θ_c, ξ diverges as P increases to a critical value P_c. This behavior is characteristic of a depinning transition.[21]

The static interfaces produced as P increases to P_c are much smoother for $\theta < \theta_c$. One way of characterizing them is through their scaling properties. We find that interfaces are self-affine with a roughness exponent of 0.75 ± 0.04 below θ_c, and self-similar with a fractal dimension characteristic of percolation above θ_c. Recent experiments[14] find a similar roughness exponent (0.73 ± 0.03) for W invasion, and the percolation character of NW invasion is well established. Because the interfaces are self-affine below θ_c, there is a well-defined average surface normal for the interface. Thus the large l limit of the surface-normal correlation function [Eq. (9)]

has a nonzero value which increases as θ decreases.[9]

Another indication of smoother growth below θ_c is a marked decrease in the amount of trapped fluid. For an $L = 1000$ realization of system A the fraction of trapped fluid is a few percent at 45°, and two orders of magnitude smaller at 25°.

A more exciting discovery is that the pressure needed to initiate flow depends on the average curvature of the interface. This reflects the cooperative nature of invasion below θ_c. Suppose one starts from a random initial ring. Increasing P leads initially to small rearrangements of the interface. There is a final stable finite interface with radius of gyration R at some pressure P_f. Further increases in P cause flooding of the entire system; it is not possible to construct a stable percolating interface. We find that the average value of P_f satisfies $P_f = P_c + \Gamma/R$, where P_c is the pressure for flooding from an *infinite* interface and Γ has the dimensions of a surface tension. Indeed, an effective macroscopic surface tension would have exactly this effect on the pressure needed for flow. The difference is that a true surface tension would be able to decrease the invaded area as well as limit its expansion. This effective surface tension may be responsible for the scaling of viscous finger widths with velocity.[9,13]

The phase diagram shown in Fig. 1 summarizes the values of the critical percolating or depinning pressures found for system A. In the region labeled "static," there are many possible stable interfaces. In the region labeled "moving," infinite interfaces would grow indefinitely. Above θ_c, one may think of this as being above the percolation threshold. Below θ_c, the divergence of the correlation length ξ at P_c implies that the entire interface determines the onset of growth. As discussed above, the pressure required to initiate flow depends on the curvature of the interface.

IV. ANALYSIS OF LOCAL INSTABILITIES

To understand the divergence of $\bar{w}$ at θ_c, we examine how the different microscopic growth mechanisms change in importance as θ decreases. Figure 16 shows the fraction of bursts, touches, and overlaps which occur during growth at P_c in system A. As noted above, almost all growth in the NW limit is due to bursts; only for

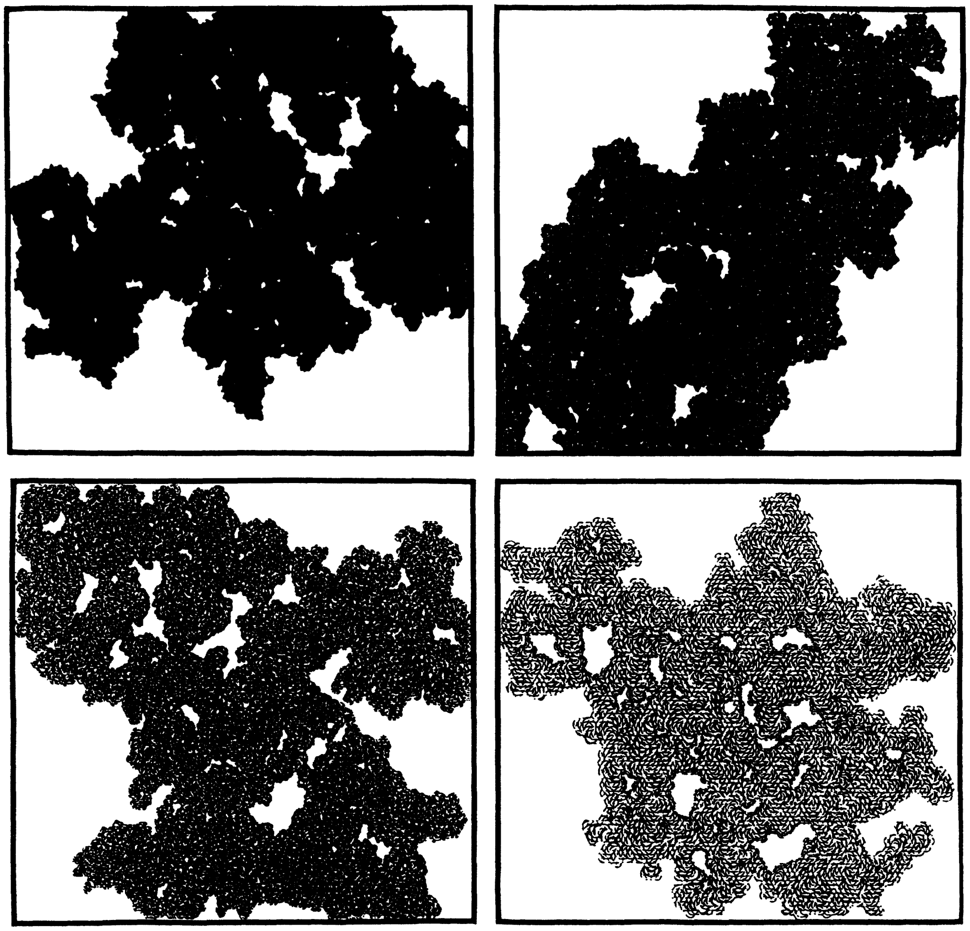

FIG. 15. Scale invariance of invasion patterns as $\theta \rightarrow \theta_c$. The top left figure corresponds to $L = 800$, $\bar{w} \simeq 79a$, and $\theta = 56°$. The top right figure corresponds to $L = 400$, $\bar{w} \simeq 39a$, and $\theta = 59°$. The bottom left figure is for $L = 200$, $\bar{w} \simeq 20a$, and $\theta = 62°$. The bottom right figure is for $L = 100$, $\bar{w} \simeq 10a$, and $\theta = 70°$.

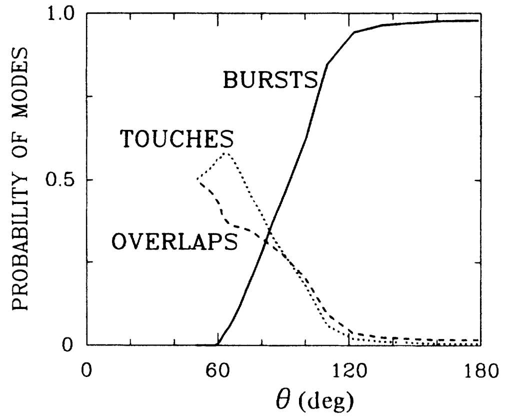

FIG. 16. Relative importance of various growth mechanisms at P_c in system A as a function of the contact angle.

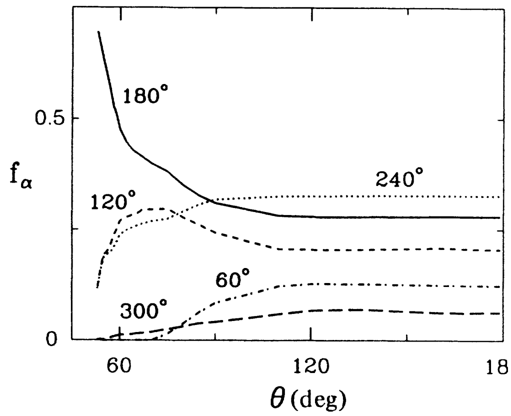

FIG. 17. Fraction f_α of each interfacial angle α on percolating interfaces in system A.

$\theta < 120°$ do other mechanisms begin to play a role. The widest throats always burst at the lowest P. Since the hierarchy of throat widths remains the same, the invaded pattern is nearly unchanged for $\theta > 120°$. Only the value of P_c is affected (Fig. 1). Bursts are well described by percolation models, and thus so are the invaded pattern, its dependence on starting ring, etc. (see Sec. III A).

As θ decreases below 120°, overlaps and touches rise rapidly in importance. Below about 90° they dominate bursts, and the invaded pattern loses all similarity to the NW pattern. The finger width begins to increase rapidly. Bursts no longer occur at all for θ within about 10° of θ_c. Since overlaps and touches are not well described by percolation models, many aspects of the growth change. For example, the invaded pattern becomes more sensitive to the position and size of the initial starting ring, as well as the sequence of growth pressures (Sec. III B).

As discussed above, the pressure for overlap is smallest when the interface makes the most acute angle (small α). As θ decreases, overlaps at larger and larger values of α occur before bursts or touches. Removing regions with small α produces smoother and smoother interfaces.

The smoothing action of overlaps is demonstrated in Fig. 17 for system A. The fraction f_α of interfacial angles with $\alpha = n \times 60°$ was calculated for large stable interfaces at each value of θ. Arcs between non-nearest neighbors can produce different values of α, but the fraction of such bonds was negligible.

In the NW limit both acute and obtuse angles occur in roughly equal proportions. There is a substantial fraction ($\sim 10\%$) of $\alpha = 60°$ bond angles. As θ decreases, there is a sharp reduction in the fraction of 60° bonds. For $\theta < 75°$ they are completely eliminated. Because the interface is large and self-avoiding, the number of $\alpha = 120°$ bonds must be balanced by 240° and 300° bonds. As θ decreases to θ_c, the fraction of these bonds decreases, and the interface contains an increasing fraction of straight, $\alpha = 180°$ segments.

In the above discussion we have focused on system A. In all systems the approach to θ_c is heralded by an increase in the probability of overlaps. However, there are differences in the details of growth statistics (Fig. 16). In system B, bursts remain important down to θ_c. The most dense system, C, shows pronounced structure in the growth statistics; for a narrow range of θ (55°–65°) about 95% of growth is by touches. A corresponding peak in $\bar{w}$ is seen in Fig. 12. Touches should continue to increase in importance as porosity decreases. Since they do not reflect cooperation by neighboring arcs they should not lead to a divergence in $\bar{w}$. It is possible that by superseding overlaps they may depress θ_c or even remove the transition in some systems.

Let us now discuss a more detailed characterization of the relevance of various instabilities to the creation of a percolating pattern above θ_c. Rather than looking at the fraction of each type of instability during growth, we consider the fraction of all possible local configurations which are unstable to each mode at a given P. The typical behavior is as follows. Below a lower bound P_l, a given mode is inactive: There are no local configurations which are unstable. Above P_l, the fraction of configurations which are unstable to the given mode grows monotonically, until it saturates at some upper bound P_u. The saturating fraction is generally unity, but may be smaller. (For example, since arcs at pressures greater than the bursting pressure are represented by the critical arcs, there is no change in the probabilities for other mechanisms once bursts have saturated.) Since the interesting region is where the probability changes, we focus on the pressure derivatives ρ of the probabilities. These derivatives can be interpreted as the number of new unstable local configurations in a unit pressure interval, or a density of instabilities.

Figure 18 compares instability densities for system A in the NW limit ($\theta = 179°$), and near θ_c ($\theta = 50°$). All densities were calculated for arcs connecting disks at nearest-neighbor positions, since these account for almost all of the growing interface. Statistics on 10 000 local configurations were used. In the NW limit, only bursts are unstable for $P < P_c$. Integrating ρ to P_c yields a fraction 0.71 of unstable bonds as mentioned in Sec. III A. At $\theta = 50°$, the relevant mechanisms are touch, overlap at $\alpha = 120°$, and overlap at $\alpha = 180°$. Bursts start to be relevant only for $P > P_c$, while overlaps at $\alpha = 60°$ are all

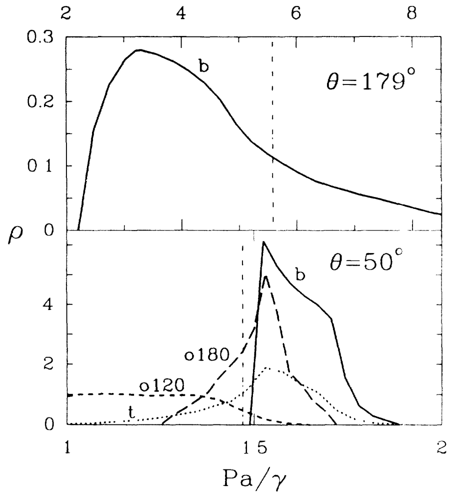

FIG. 18. Probability density of instabilities as a function of pressure at the indicated values of θ in system A. Curves are labeled by b for bursts, t for touches, and $o\alpha$ for overlaps at interfacial angle α. Vertical lines indicate P_c (obtained by extrapolation for $\theta=50°$). The densities are pressure derivatives of the fraction of arcs which are unstable and were calculated numerically using 10^4 local configurations.

unstable at much lower pressures. Despite the clear difference between the densities for the two values of θ shown, it is not obvious how the diverging finger width arises.

System B turns out to be much simpler to analyze as testified by Fig. 19. In the vicinity of P_c and θ_c there are only two relevant modes: bursts and overlaps at $\alpha=120°$. Just above θ_c, e.g., at $\theta=72°$ (Fig. 19), P_c lies in a region where the densities of the two modes overlap. For $\theta<69.715°$ a gap between the two densities opens up. It is easy to show that growth can no longer be percolation-like in this range of θ.

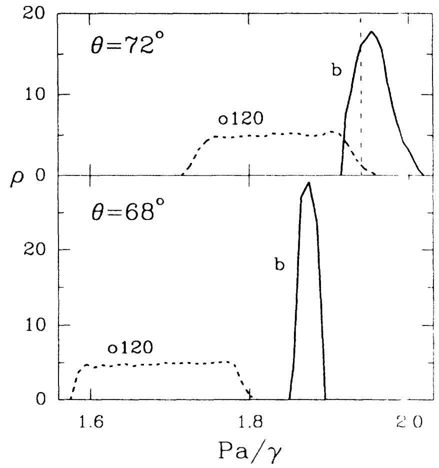

FIG. 19. Similar to Fig. 18 but for system B. The top and bottom panels are for θ above and below θ_c, respectively. A gap between densities for bursts and overlaps at $\alpha=120°$ occurs for $\theta\leq 69.715°$.

Consider any initial interface. For P in the gap between densities for bursts and overlaps all bond angles less than 180° are unstable. Thus the only stable interfaces are infinite straight lines or finite convex shapes such as hexagons. If P is increased until the first burst occurs, a small segment of the straight interface will move forward. Two new 120° bonds will be formed on either side. Since all such bonds are unstable, they will overlap, producing two new 120° arcs farther along the line. These will also be unstable, producing new arcs, etc. Thus as soon as P reaches the bottom of the density of bursts, the pattern will grow forever. Above 69.715°, there will always be some stable 120° bonds at pressures where some bursts are unstable. If one starts from a straight line and a single burst initiates growth, it will only be able to spread along the line until a stable 120° angle is reached on each side. The distance between these stable angles will diverge as the number of stable 120° bonds below P_c goes to zero.

This simple picture would suggest that θ_c must coincide with 69.715°. However, it is a 1D model which only considers the first row of growth. There will be arcs on this new row which are unstable against bursts. These in turn may create a new row and another. It is possible for the interface to bulge forward and surround unfavorable bonds, as long as there are not too many. This definitely occurs for system A where there is no gap and some 120° bonds are always stable at P_c. System B may be different. We cannot determine whether $\theta_c=69.715$ or whether it is slightly larger. In the former case, the critical behavior may be different than for system A. The disorder in system B is much smaller, and we can think of it as analogous to a clock model with well-defined separate densities for each discrete angle. System A is so disordered that some 180° bonds are unstable before other 120° bonds. One may think of this as washing out the lattice anisotropy and thus changing the order parameter from discrete to continuous. More work is needed to establish whether these systems are in different universality classes.

Systems C and D appear to be in the same class as system A, because no gap opens in the density of instabilities near θ_c. However, the instabilities which dominate growth are different in the two systems. In system C, overlaps with $\alpha=120°$ and touches are important. In system D, stable arcs connect both nearest and next-nearest neighbors. Thus α takes values $n\times 45°$. The important mechanisms near θ_c are overlap at 135° and 180°.

These results indicate the rich variety of mechanisms which can produce a divergence in $\bar{w}$. The only unifying feature is that overlaps must be present to smooth the interface.

V. CONCLUDING REMARKS

In conclusion, we have presented a detailed study of fluid invasion of model 2D porous media. For θ greater than a critical angle θ_c, growth is characteristic of percolation. The fractal dimension of the invaded pattern in our simulations is consistent with normal percolation.[10] Previous studies[11] concluded that trapping lowered d_f to a nonuniversal value. However, these studies were all for site percolation models and smaller systems. More work is needed to determine when trapping may produce nonuniversal behavior.

As $\theta \rightarrow \theta_c$ the dominant local growth mode changes from bursts to overlaps. Since overlaps are cooperative, this leads to a diverging length over which invasion is correlated. This was quantified by measuring the width of fingers in the percolating pattern. Below θ_c the entire interface becomes correlated and the fluid advances in a uniform flood. The existence of the transition from percolation to uniform floods appears to be independent of the exact pore geometry. However, the value of θ_c varies with porosity. Examination of the probabilities of local growth modes indicates the origin of the transition, and suggests that there may be two different universality classes.

We have studied this transition in the lowest dimension where it can be defined. The interface is 1D, and will be roughened by arbitrarily weak disorder. By analogy with equilibrium critical phenomena, we expect the transition to also occur in higher dimensions. Indeed, the greater connectivity of interfaces in 3D should facilitate divergence of the finger width, leading to higher values of θ_c. One may also expect smoother advancing fronts below θ_c.

Experiments[4-6,8,12,13] in the NW and W limits show a marked change in growth patterns, which is consistent with our results. However, measurements over a range of contact angles are needed to establish the existence of a critical phase transition. Recent studies[22] have varied θ by using varying mixtures of ethanol and methanol (alcohols) for one of the fluids, and hexadecane (an oil) as the second. These studies indicate a critical transition does occur, and that θ_c is larger in 3D than in 2D. A sharp rise occurs in $\bar{w}$ as $\theta \rightarrow \theta_c$, but more work is needed to determine the critical behavior.

ACKNOWLEDGMENTS

We thank J. R. Banavar, A. Dougherty, J. P. Gollub, E. Herbolzheimer, N. Martys, P. Meakin, M. Murat, J. P. Stokes, and D. A. Weitz for useful discussions, and N. Martys for help in analyzing the fractal dimension of clusters. Support from the National Science Foundation through Grant No. DMR-8553271 and matching funds from the Exxon Education Foundation is gratefully acknowledged. Work stations donated by SUN Microsystems enabled us to perform the simulations described. One of us (M.O.R.) also acknowledges support from the Sloan Foundation.

---

[*] Permanent address: Institute of Physics, Polish Academy of Sciences, 02-668 Warsaw, Poland.

[1] P.-Z. Wong, Phys. Today **41**, No. 12, 24 (1988).

[2] J. Feder, *Fractals* (Plenum, New York, 1988).

[3] E. Ben-Jacob, R. Godbey, N. D. Goldenfeld, J. Koplik, H. Levine, T. Mueller, and L. M. Sander, Phys. Rev. Lett. **55**, 1315 (1985).

[4] R. Lenormand and C. Zarcone, Phys. Rev. Lett. **54**, 2226 (1985); R. Lenormand, C. Zarcone, and A. Zorr, J. Fluid Mech. **135**, 337 (1983).

[5] R. Lenormand and S. Bories, C. R. Acad. Sci. Ser. B **291**, 279 (1980).

[6] R. Chandler, J. Koplik, K. Lerman, and J. F. Willemsen, J. Fluid Mech. **119**, 249 (1982).

[7] L. Patterson, Phys. Rev. Lett. **52**, 1621 (1984).

[8] K. Maloy, J. Feder, and T. Jossang, Phys. Rev. Lett. **55**, 2688 (1985).

[9] N. Martys, M. Cieplak, and M. O. Robbins (unpublished).

[10] See, for example, D. Stauffer, *Introduction to Percolation Theory* (Taylor and Francis, London, 1985).

[11] D. Wilkinson and J. F. Willemsen, J. Phys. A **16**, 3365 (1983).

[12] R. Lenormand and C. Zarcone, in *Proceedings of the Fifty-Ninth Annual Technological Conference and Exhibition of the Society of Petroleum Engineers, Houston, Texas, September, 1984* (Society of Petroleum Engineers, Richardson, TX, 1984); R. Lenormand, C. Zarcone, and E. Touboul, J. Fluid Mech. **187**, 165 (1988).

[13] J. P. Stokes, D. A. Weitz, J. P. Gollub, A. Dougherty, M. O. Robbins, P. M. Chaikin, and H. M. Lindsay, Phys. Rev. Lett. **57**, 1718 (1986).

[14] M. A. Rubio, C. Edwards, A. Dougherty, and J. P. Gollub, Phys. Rev. Lett. **63**, 1685 (1989).

[15] W. G. Anderson, J. Petrol. Tech. **39**, 1453 (1987).

[16] M. Cieplak and M. O. Robbins, Phys. Rev. Lett. **60**, 2042 (1988).

[17] A fluid interface intersects a solid at a θ fixed by the balance of surface energies; see P. G. DeGennes, Rev. Mod. Phys. **57**, 827 (1985).

[18] L. Schwartz and S. Kimminau, Geophysics **52**, 1401 (1982).

[19] B. Dubuc, J. F. Quiniou, C. Roques-Carmes, C. Tricot, and S. W. Zucker, Phys. Rev. A **39**, 1500 (1989).

[20] The value of $\nu \simeq 2.3$ given by us in Ref. 16 was based on fewer data points. The upper limit of the radii range for systems A and D was incorrectly listed as 0.48 instead of 0.49.

[21] D. S. Fisher, Phys. Rev. Lett. **50**, 1486 (1983); Phys. Rev. B **31**, 1396 (1985).

[22] J. P. Stokes, A. Kushnick, and M. O. Robbins (unpublished).

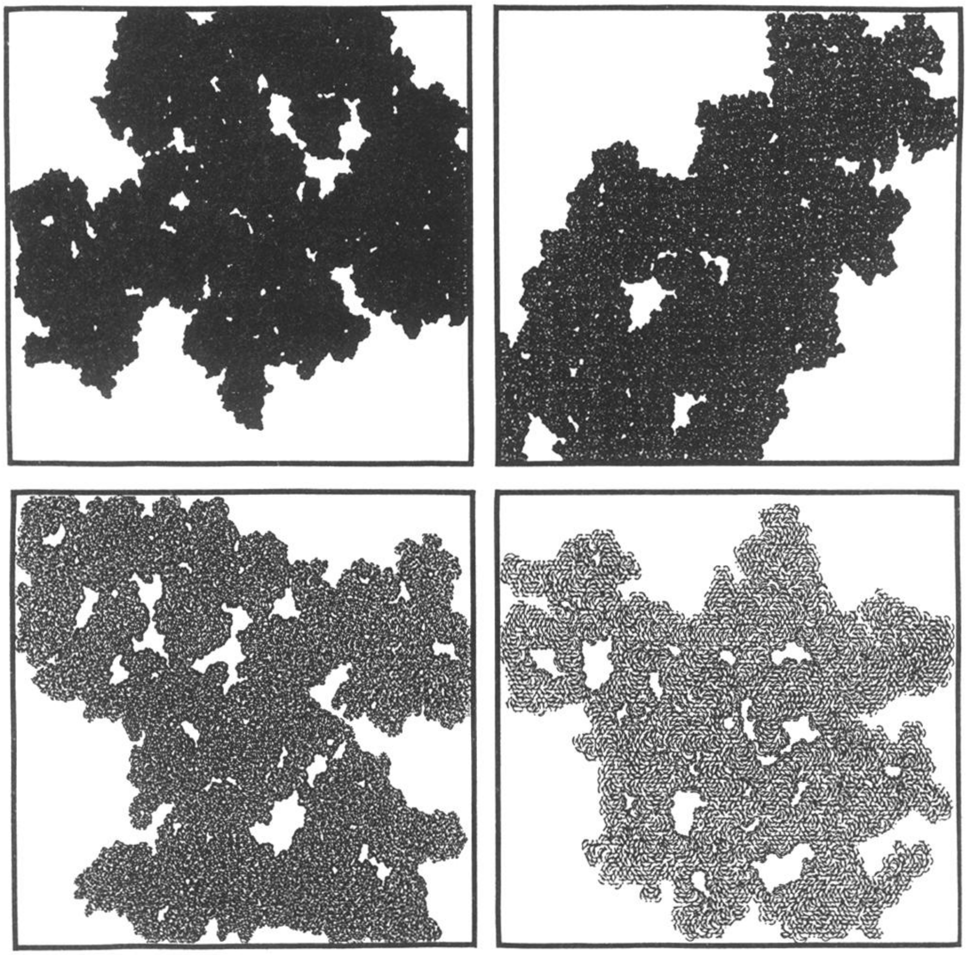

FIG. 15. Scale invariance of invasion patterns as $\theta \rightarrow \theta_c$. The top left figure corresponds to $L = 800$, $\overline{w} \simeq 79a$, and $\theta = 56°$. The top right figure corresponds to $L = 400$, $\overline{w} \simeq 39a$, and $\theta = 59°$. The bottom left figure is for $L = 200$, $\overline{w} \simeq 20a$, and $\theta = 62°$. The bottom right figure is for $L = 100$, $\overline{w} \simeq 10a$, and $\theta = 70°$.